Saroha *et al. Energy Mater.* **2025**, *5*, 500089
DOI: 10.20517/energymater.2024.279

Energy Materials

Article

Open Access

Check for updates

Polysulfide barrier comprising bismuth selenide nanocrystals well anchored within N-doped carbon microspheres for stable Li-S batteries

Rakesh Saroha[1,2,#], Jae Seob Lee[1,3,#], Sung Woo Cho[1,#], Chungyeon Cho[4,*], Jin-Sung Park[2,5,*], Jung Sang Cho[1,6,7,*]

[1]Department of Engineering Chemistry, Chungbuk National University, Cheongju 28644, Republic of Korea.
[2]Department of Materials Science and Engineering, Ajou University, Suwon 16499, Republic of Korea.
[3]Department of Materials Science and Engineering, Korea University, Seoul 02841, Republic of Korea.
[4]Department of Biomedical Materials Science, Jeonbuk Advanced Bio-convergence Academy, Wonkwang University, Iksan 54538, Republic of Korea.
[5]Department of Energy Systems Research, Ajou University, Suwon 16499, Republic of Korea.
[6]Biomedical Research Institute, Chungbuk National University Hospital, Cheongju 28644, Republic of Korea.
[7]Advanced Energy Research Institute, Chungbuk National University, Cheongju 28644, Republic of Korea.
[#]Authors contributed equally.

[*]**Correspondence to:** Prof. Chungyeon Cho, Department of Biomedical Materials Science, Jeonbuk Advanced Bio-convergence Academy, Wonkwang University, 460 Iksan-daero, Jeonbuk-do, Iksan 54538, Republic of Korea. E-mail: cncho37@wku.ac.kr; Prof. Jin-Sung Park, Department of Materials Science and Engineering, Ajou University, 206 Worldcup-ro, Yeongtong-gu, Gyeonggi-do, Suwon 16499, Republic of Korea. E-mail: jinsung@ajou.ac.kr; Prof. Jung Sang Cho, Department of Engineering Chemistry, Chungbuk National University, 1 Chungdae-ro, Seowon-Gu, Chungcheongbuk-do, Cheongju 28644, Republic of Korea. E-mail: jscho@cbnu.ac.kr

How to cite this article: Saroha, R.; Lee, J. S.; Cho, S. W.; Cho, C.; Park, J. S.; Cho, J. S. Polysulfide barrier comprising bismuth selenide nanocrystals well anchored within N-doped carbon microspheres for stable Li-S batteries. *Energy Mater.* **2025**, *5*, 500089. https://dx.doi.org/10.20517/energymater.2024.279

Received: 5 Dec 2024 **First Decision:** 26 Dec 2024 **Revised:** 6 Jan 2025 **Accepted:** 22 Jan 2025 **Published:** 22 Apr 2025

Academic Editor: Jiaqi Huang **Copy Editor:** Ping Zhang **Production Editor:** Ping Zhang

Abstract

The development of functional interlayers to effectively anchor lithium polysulfide and enhance the integrity of sulfur cathodes in lithium-sulfur (Li-S) batteries has received significant global consideration. However, identifying an interlayer that is both highly conductive and structurally robust remains a major challenge. This study presents the synthesis of three-dimensional nitrogen-doped carbon microspheres embedded with bismuth selenide nanocrystals (referred to as "three-dimensional (3D) Bi_2Se_3@N-C" microspheres) and evaluates their role as a polysulfide barrier for enhanced Li-S battery performance. The embedded Bi_2Se_3 nanocrystals within the microspheres provide numerous active spots for chemical captivity and electrocatalytic transformation of lithium

polysulfide species. Moreover, the N-doped carbon framework facilitates speedy transfer of charge moieties, resulting in faster redox activity. Correspondingly, cells paired with 3D Bi_2Se_3@N-C microsphere modified separators exhibit excellent rate capability (297 mA h g^{-1} at 2.0 C-rate) and prolonged stable cycling performance at different C-rates (863 mA h g^{-1} after 100 cycles at 0.1 C, 440 mA h g^{-1} after 200 cycles at 0.5 C, and 219 mA h g^{-1} after 500 cycles at 2.0 C). The cell demonstrates satisfactory cycling performance retaining 57% of its capacity after 200 cycles when the active material loading was raised to 3.5 mg cm^{-2}, confirming the practical feasibility of the prepared nanostructure. The detailed physical and electrochemical results presented in this study offer valuable perceptions for the expansion of structurally superior, conductive, and easily scalable nanostructures for various energy storage demands.

Keywords: Lithium-sulfur batteries, polysulfide barrier, N-doping, carbon microsphere, metal selenide

INTRODUCTION

Lithium-sulfur batteries (LSBs) have garnered significant attention due to their high energy density (calculated at 2,600 Wh kg^{-1}), plentiful sulfur (S) resources, and low cost[1-3]. Sulfur enables a multiple-electron ($2e^-$) redox activity, offering a high capacity (theoretical value of 1,675 mA h g^{-1} at an average potential of approximately 2.2 V versus Li/Li^+[4,5]. However, their commercialization is hindered by several challenges, including the poor electrical conductivity of sulfur (5×10^{-28} S m^{-1}) and lithium sulfide (Li_2S_x; x = 1 or 2, ~10^{-11} S m^{-1}), the "shuttle effect" caused by the dissolution and migration of intermediate lithium polysulfide (LiPS) species (Li_2S_x, $4 \leq x \leq 8$), significant volume change (~80%) during lithiation related to density differences between S (2.07 g cm^{-3}) and end product (Li_2S; 1.66 g cm^{-3}), and the instability of lithium metal anodes during redox processes[6,7]. To address these issues, researchers have explored strategies such as scheming carbon-based frameworks to confine sulfur[8-11], restraining LiPSs through physical or chemical interactions[12,13], stabilizing lithium metal anodes[14,15], accommodating volumetric changes[16,17], and optimizing electrolytes[18,19]. While these approaches have effectively improved LSB performance by suppressing polysulfide diffusion and confining polysulfides within the cathode domain, the complex synthesis of sulfur-carbon nanocomposites limits scalability. Furthermore, these processes often reduce the sulfur content in the composites, thereby diminishing energy density and electrochemical performance, posing significant barriers to large-scale implementation. An emerging strategy to address the challenges involves incorporating additional interlayer components into LSBs, either as a free-standing structure or coatings on the separator within the cell. This approach has gained significant attention due to its simplicity and practical applicability. The interlayer realizes multiple functions, including the effective confinement of polysulfides and facilitating rapid charge diffusion. To meet these requirements, the interlayer material should possess polar characteristics, offering abundant active chemisorption sites to anchor polysulfide and prevent their diffusion.

In this context, our group and others have demonstrated that separators functionalized with metal selenides exhibit promising electrochemical performance in LSBs, owing to their excellent electrocatalytic activity towards LiPS[20-23]. Despite the extensive exploration of chalcogenides, one particularly intriguing candidate has been largely overlooked: bismuth selenide (Bi_2Se_3). This material belongs to the $A_2^{V}B_3^{VI}$ class (A = Sb, Bi; B = Se, Te) of degenerated n-type semiconductor material, characterized by a low bandgap of 0.3 eV[24-26]. While it has attracted significant interest in fields such as thermoelectric and optoelectronic devices, its potential application in LSBs remains unexplored[27]. The n-type electronic behavior of Bi_2Se_3 arises from Se deficiencies, which behave similarly to electron donors. Bi_2Se_3 features a layered structure composed of covalently stacked Se-Bi-Se-Bi-Se atomic layers. This unique structure, combined with its high electrical conductivity and mutable valences of Bi and Se, offers a significant catalytic perspective.

Here, we disclose the synthesis of three-dimensional (3D) nitrogen-doped carbon microspheres embedded with bismuth selenide nanocrystals (3D Bi_2Se_3@N-C microspheres) using a scalable spray pyrolysis procedure trailed by a selenization process. The potential of these prepared microspheres as an effective polysulfide barrier to enhance reaction kinetics in Li-S batteries is systematically evaluated. The embedded Bi_2Se_3 nanocrystals within the microspheres provide abundant chemisorption sites, enabling efficient chemical captivity and transformation of LiPS species. Moreover, the N-doped carbon framework ensures rapid charge transfer, facilitating faster redox processes. Electrochemical evaluations reveal that 3D Bi_2Se_3@N-C microsphere coated separators exhibit excellent rate competence and stable cycling across different C-rates (0.1 C, 0.5 C, and 2.0 C). Notably, even at high active material loading (3.5 mg cm^{-2}), the cell demonstrates robust cycling stability, highlighting the effectiveness of this material design.

EXPERIMENTAL

Synthesis of 3D Bi_2Se_3@N-C microspheres

Synthesis of 3D nitrogen-doped carbon (N-C) microspheres comprising well-grafted bismuth selenide nanocrystals (denoted as "3D Bi_2Se_3@N-C" microspheres) is achieved using an easily scalable spray pyrolysis technique assisted with a selenization process and applied as a multifunctional polysulfide barrier facing towards the sulfur cathode. Initially, spray solution was prepared using 0.025 M (2.42 g) of bismuth nitrate pentahydrate [$Bi(NO_3)_3{\cdot}5H_2O$, Junsei Chemical Co., Ltd. (JUNSEI), M_w = 485.07] dispersed in a blend of distilled water (100 mL) and nitric acid (15 mL, HNO_3, JUNSEI, M_w = 63.01), resulted in a transparent solution. To the above solution, 0.05 M (1.71 g) of sucrose [$C_{12}H_{22}O_{11}$, DAEJUNG Chemicals Metals (DAEJUNG), M_w = 342.3] as a carbon source and 1.5 g of polyvinylpyrrolidone (PVP, M_w = 40,000, DAEJUNG) as a nitrogen source were also added. The solution was allowed to stir gently overnight at ambient conditions. The obtained solution was transferred to an ultrasonic atomic nebulizer coupled with a vertically positioned quartz tube reactor. The ultrasonic nebulizer generates aqueous droplets which are subsequently passed through the preheated quartz tube reactor operated at 400 °C. A constant gas flow (N_2, 20 L min^{-1}) was maintained throughout the process. The as-sprayed powder was collected carefully and further heat-treated (selenization) at 350 °C for 6 h in a slightly reductive atmosphere (4% of H_2/Ar) at a ramp rate of 5 °C min^{-1}. Excess selenium powder (Se, 99.5%, SAMCHUN, 200 mesh) was used for complete selenization of the as-sprayed powder through the H_2Se gas production.

RESULTS AND DISCUSSION

To validate the successful synthesis of 3D Bi_2Se_3@N-C microspheres, detailed physical characterizations were conducted at each step of the synthesis process. Field emission scanning electron microscopy (FE-SEM) and X-ray diffraction (XRD) analyses of the as-sprayed Bi-salt/PVP/Sucrose composite microspheres are presented in Supplementary Figure 1. The low-magnification FE-SEM micrograph [Supplementary Figure 1A] shows the formation of 3D spherical microspheres (average diameter = 1.3 μm). Additionally, the prepared powder appears uniform and free from agglomeration. The magnified FE-SEM micrograph [Supplementary Figure 1B] further reveals a smooth microsphere surface devoid of any foreign deposits, suggesting complete encapsulation of the Bi-salt within the microspheres. The XRD pattern [Supplementary Figure 1C] shows the absence of any sharp diffraction peaks, indicating the amorphous nature of the as-prepared sample.

The as-sprayed Bi-salt/PVP/Sucrose composite microspheres were subjected to a selenization process under a mildly reductive atmosphere (4% of H_2/Ar) at 350 °C for 6 h. The physical characterization results of the resulting microspheres are presented in Figure 1. The FE-SEM micrograph [Figure 1A] discloses that the spherical morphology of the selenized microspheres was retained (average diameter = 1.1 μm) even after the selenization process. Furthermore, the high-magnification FE-SEM image [inset of Figure 1A] reveals

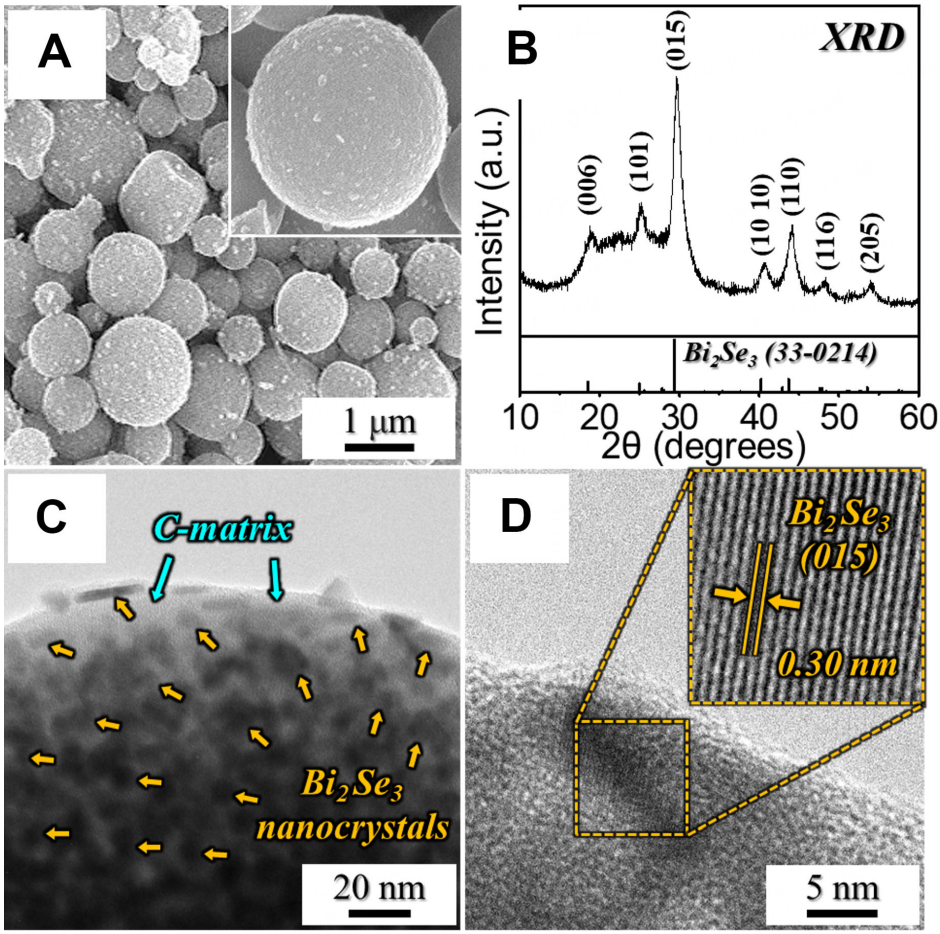

Figure 1. (A) FE-SEM micrograph; (B) XRD profile; (C) TEM picture; and (D) HR-TEM image of the 3D Bi_2Se_3@N-C microspheres. FE-SEM: Field emission scanning electron microscopy, XRD: X-ray diffraction, TEM: transmission electron microscopy, HR-TEM: high-resolution transmission electron microscopy.

significant changes in surface characteristics. Unlike the smooth surface of the as-sprayed sample, the selenized microspheres exhibit a rougher texture, with the surface covered by well-formed nanocrystals, likely Bi_2Se_3. This observation aligns with the XRD analysis shown in Figure 1B, where sharp, distinct diffraction peaks correspond to the rhombohedral crystal structure of Bi_2Se_3 with a $R\bar{3}\,m$ space group. Moreover, the average crystallite size of Bi_2Se_3 was *cal.* about 7.1 nm using Scherrer's equation by considering the high-intensity reflection of the (110) plane for Bi_2Se_3. Notably, a broad peak centered in the 2θ range of 20°-25° is attributed to the carbonaceous species derived from sucrose and PVP. The presence of PVP also ensures N-doping within the carbonaceous framework owing to the presence of N-containing organic components. A low-magnification transmission electron microscopy (TEM) image [Supplementary Figure 2A] confirms the spherical morphology observed in the FE-SEM results. Furthermore, the existence of well-developed Bi_2Se_3 nanocrystals (dark patches) on the surface and within the carbon framework (grey region) of the prepared microsphere is clearly evident, as highlighted in Figure 1C. High-resolution TEM [Figure 1D] reveals Bi_2Se_3 nanocrystal with size of approximately 7 nm, which aligns with crystallite size calculated using Scherrer's equation employing XRD pattern. Moreover, inset of Figure 1D displayed distinct lattice fringes with a separation of 0.30 nm, corresponding to the (015) diffraction plane of the Bi_2Se_3 phase. This result, along with the XRD findings, aligns with the selected area electron diffraction (SAED) pattern [Supplementary Figure 2B], which displays continuous diffraction rings corresponding to various

Bi_2Se_3 planes. Elemental dot mapping images [Supplementary Figure 2C] confirm the uniform dispersal of Bi, Se, C, and N elements all over the microspheres, verifying the successful synthesis of Bi_2Se_3@N-C microspheres. Notably, the high density of N-element dots is aligned with the elemental analysis (EA) results (discussed shortly), further supporting the presence of nitrogen doping.

Based on the discussion above, Scheme 1 illustrates the detailed formation mechanism of the 3D Bi_2Se_3@N-C microspheres. Aqueous droplets, generated by the ultrasonic atomic nebulizer, contained uniformly distributed sucrose, PVP, and Bi-salt, as depicted in Scheme 1-①. These droplets were consequently gone through a vertically aligned quartz tube, stabilized at 400 °C, under a flowing Ar carrier gas. This process dried the droplets, transforming the precursor into a Bi-salt/PVP/sucrose composite [Scheme 1- ②]. The resulting powders were then underwent selenization at 350 °C for 6 h. Elemental selenium was employed to generate H_2Se gas. During selenization, the PVP polymer (as a nitrogen source) and sucrose decomposed gradually, forming an N-doped C matrix, as illustrated in Scheme 1-③. This N-C framework offers structural robustness and numerous conductive corridors for electrons within the microspheres. Concurrently, the Bi-salt precursor was converted into the stoichiometric Bi_2Se_3 phase, completing the formation of the 3D Bi_2Se_3@N-C microspheres. Notably, the yield during the spray pyrolysis and subsequent selenization process was *cal.* approximately 51% and 55%, respectively [Supplementary Figure 3A-D]. The as-prepared 3D Bi_2Se_3@N-C microspheres were applied as multifunctional polysulfide interlayers through a slurry-coating process, as shown in Scheme 1-④.

The surface composition and bonding states within the 3D Bi_2Se_3@N-C microspheres were assessed via X-ray photoelectron spectroscopy (XPS). The survey profile presented in Figure 2A reveals the occurrence of photoelectron signals for Bi 4*f*, Se 3*d*, C 1*s*, and N 1*s*, confirming the existence of elements in the nanostructure. The Bi 4*f* expanded XPS spectrum in Figure 2B displays two well-fitted peaks: Bi $4f_{7/2}$ at 157.2 eV and Bi $4f_{5/2}$ at 162.2 eV, with a spin-orbit separation of 5 eV, indicating the presence of Bi in the +3 oxidation state within the prepared nanostructure[28,29]. Besides, peaks at 157.8 eV and 163.0 eV correspond to the Bi_2O_3 species, which likely formed due to surface oxidation during data acquisition[30,31]. The magnified Se 3*d* spectrum in Figure 2C shows two distinct peaks at 52.4 eV and 53.2 eV, corresponding to Se $3d_{5/2}$ and Se $3d_{3/2}$ electronic orbitals, respectively, which are attributed to Bi-Se bond in Bi_2Se_3[32-34]. Moreover, the broad peak at 54.1 eV is attributed to the Se-O species, indicating oxidation of the specimen surface[35,36]. The C 1*s* spectrum in Figure 2D shows three peaks at 284.1 eV, 285.3 eV, and 287.1 eV, associated with double bonded sp^2-carbon (-C=C-), single bonded sp^3-carbon (-C-N/C-C-), and polar covalent (-C-O-) bonds, respectively[37-39]. The dominant -C=C- signal suggests a carbon matrix, while the -C-N/C-C- peak reveals N-doping within the carbonaceous architecture, which enhances the conductivity of the material and offers supplementary sites for polysulfide trapping[40-42]. The N 1*s* XPS spectrum in Figure 2E further validates the N-doping, revealing three peaks at 398.1 eV, 400.5 eV, and 402.5 eV, corresponding to pyridinic, pyrrolic, and graphitic species of nitrogen, respectively[43,38]. These findings are corroborated by EA results, presented in Supplementary Table 1, which shows that the carbon and nitrogen contents are approximately 37.5 and 6.1 wt%, respectively. This confirms the successful formation of an N-C skeleton constituting the microspheres. The thermal stability of the prepared microspheres was evaluated using the thermogravimetric (TG) curve in an air atmosphere, as shown in Figure 2F, which reveals a continuous phase alteration of the selenide phase (Bi_2Se_3) to an oxide phase (Bi_2O_3), as temperature progresses. Furthermore, the N_2 adsorption-desorption analysis of 3D Bi_2Se_3@N-C microspheres was performed to measure the porosity of the microspheres [Supplementary Figure 4A and B]. The Brunauer-Emmett-Teller (BET) surface area of the 3D Bi_2Se_3@N-C microspheres was 3 $m^2 g^{-1}$, suggesting low porosity of the nanostructure. The low specific surface area of the nanostructure minimizes the consumption of electrolytes by the interlayer materials, enabling the implementation of a LSB that can

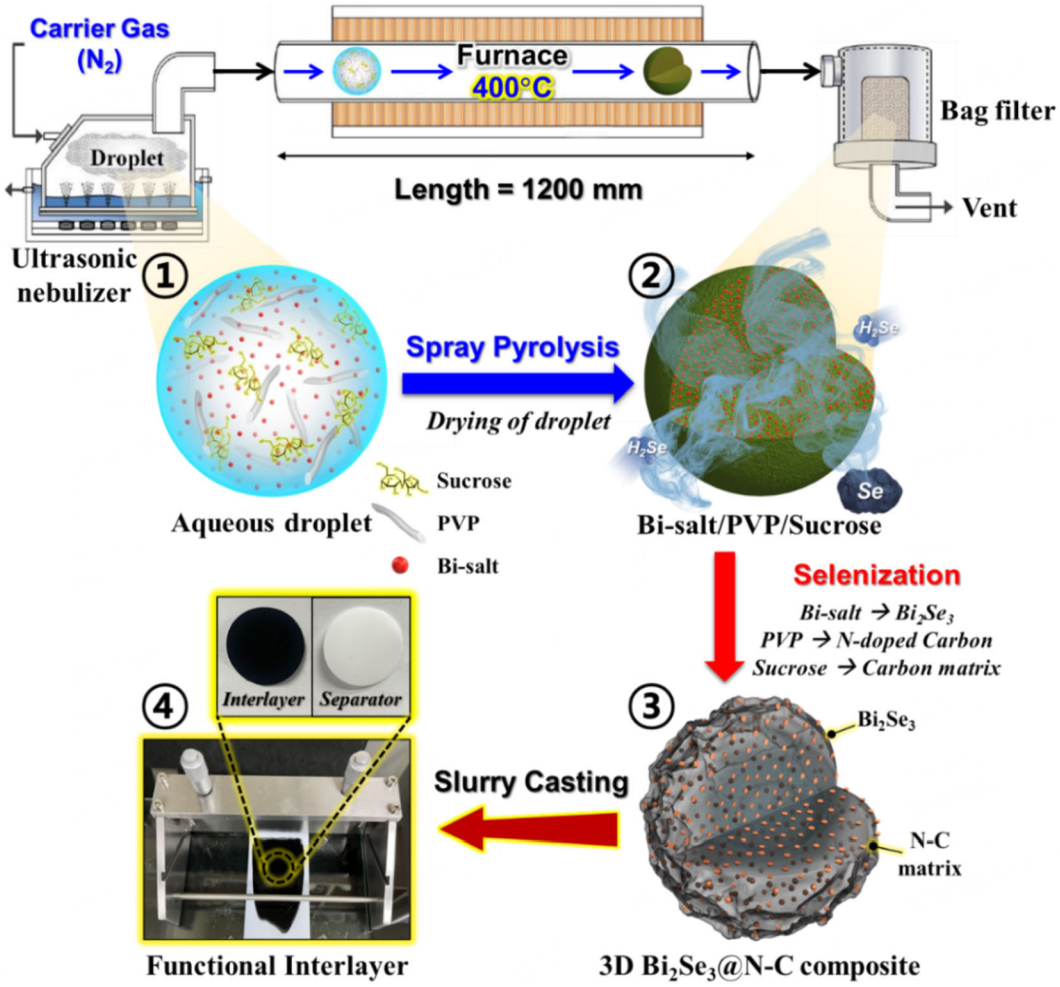

Scheme 1. Representation of the detailed synthesis route for 3D Bi_2Se_3@N-C microspheres using spray pyrolysis technique (①-③) and their utilization as multifunctional polysulfide barrier (④). 3D: Three-dimensional.

operate with a low E/S ratio.

Before evaluating the electrochemical properties of the assembled Li-S cells, the prepared multifunctional barrier and the pristine separator were subjected to physical analysis and integrity tests. Supplementary Figure 5A demonstrates a digital image of the coated separator, which appears uniform, continuous, and free from cracks. The coated separator was sliced into round disks (ϕ = 19 mm), as displayed in Supplementary Figure 5B. The thickness of the coated functional separator [Supplementary Figure 5C] and the pristine separator [Supplementary Figure 5D] was measured using a digital thickness meter, revealing a coating layer approximately 5 μm thick. Besides, the mechanical robustness of the modified separator was evaluated through folding and bending tests, as shown in Supplementary Figure 5E. Remarkably, the coated separator regained its original shape after these tests, demonstrating excellent mechanical robustness. The active loading mass of the coated separator was determined to be 5.2 mg [Supplementary Figure 5F], corresponding to a surface mass density of approximately 0.4 mg cm^{-2}. The FE-SEM micrograph of the uncoated Celgard 2400 separator, presented in Supplementary Figure 6A, reveals interconnected submicron-sized porous openings. These openings facilitate the uninterrupted transport of Li^+ ions during redox reactions and enable efficient electrolyte percolation. Conversely, the FE-SEM micrograph of the

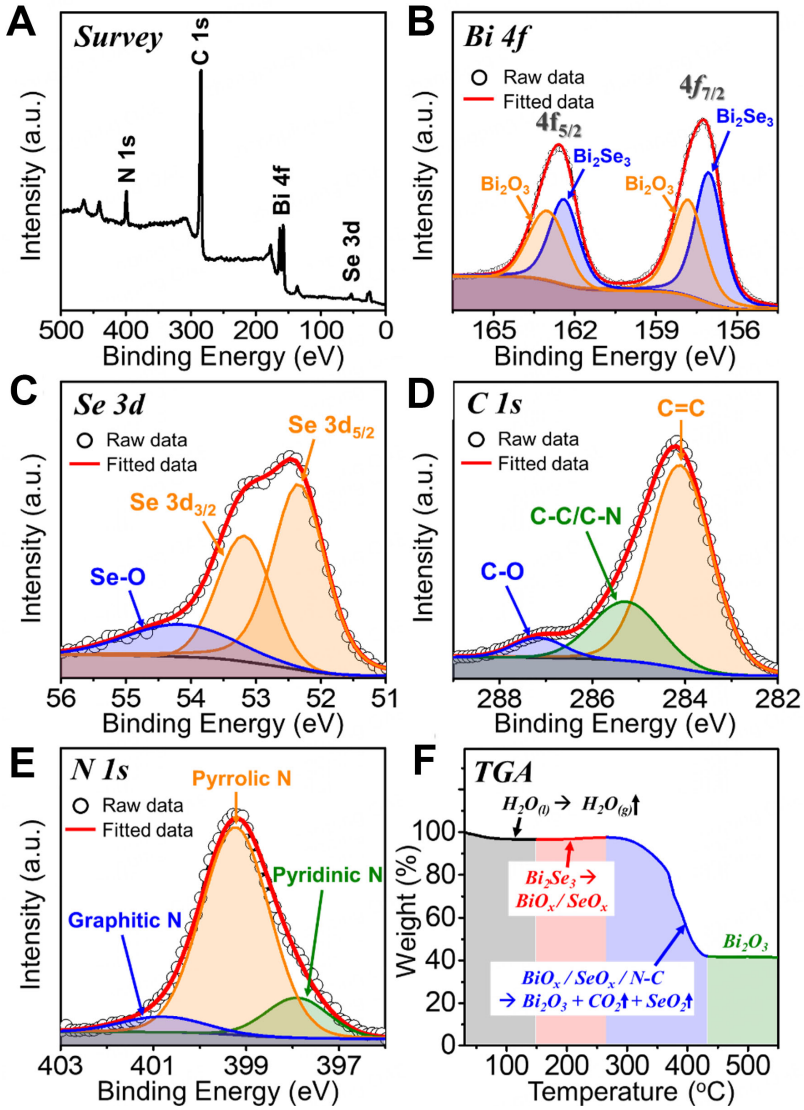

Figure 2. (A) XPS survey; (B) deconvoluted Bi 4*f* spectrum; (C) deconvoluted Se 3*d* spectrum; (D) deconvoluted C 1s spectrum; (E) deconvoluted N 1s spectrum; and (F) TG profile of 3D Bi_2Se_3@N-C microspheres in an air atmosphere. XPS: X-ray photoelectron spectroscopy, TG: thermogravimetric, 3D: three-dimensional.

functional polysulfide barrier coated with 3D Bi_2Se_3@N-C microsphere [Supplementary Figure 6B] displays a dense and uniform coating of the microspheres. Additionally, the thickness of the coating layer was observed to be approximately 5 μm, as confirmed by Supplementary Figure 6C, which aligns well with the values obtained from the digital thickness measurements. Furthermore, the coated separator was subjected to wettability tests, as shown in Supplementary Figure 7. As observed, a smaller contact angle [15.8°, Supplementary Figure 7A] for the coated separator compared to the pristine sample [39.7°, Supplementary Figure 7B] implies better wettability. Moreover, it was observed that the electrolyte absorption capability of the coated separator is approximately 63% higher than that of the pristine separator, as evident from the digital images presented in Supplementary Figure 7C-F, which clearly indicates a higher weight of the coated separator after soaking for a predetermined time in the electrolyte.

The as-prepared 3D Bi_2Se_3@N-C microspheres were engaged as a polysulfide barrier by coating them onto a commercial Celgard separator, positioned to face the regular sulfur cathode. The assembled CR2032 coin cells were initially subjected to cyclic voltammetry (CV) tests at a scan rate of 0.1 mV s^{-1}, and the first scans are presented in Figure 3A. For the cell incorporating the 3D Bi_2Se_3@N-C coated separator, the CV scan reveals two sharp and intense reduction peaks, labeled R1 and R2, centered at 2.31 V and 2.0 V, respectively. In contrast, the cell paired with a pristine separator exhibits broader and less intense reduction peaks located at 2.20 V and 1.96 V, respectively. Notably, the R1 peak corresponds to the reduction process to form high-order LiPSs (Li_2S_8 or Li_2S_6), which are further converted into middle-order polysulfides. The R2 peak signifies the subsequent reduction to form insoluble Li_2S species[44,45]. During the reverse scan, two closely spaced oxidation peaks are observed for the 3D Bi_2Se_3@N-C coated separator, representing the reverse mechanism. These peaks correspond to the oxidation of Li_2S to Li_2S_6 or Li_2S_8 at 2.38 V and further to elemental sulfur at around 2.44 V, completing the redox process[46,47]. Conversely, the cell with the pristine separator displays two unresolved oxidation peaks at significantly higher voltage values, 2.49 V and 2.52 V. It is noteworthy to mention that the cell utilizing the 3D Bi_2Se_3@N-C modified separator demonstrates the maximum redox current values, signifying enriched redox activities. This observation aligns with the individual peak voltage values reflected in Supplementary Figure 8A and respective voltage polarization values (the difference in voltage between the O and R2 peaks). Notably, the cell featuring the 3D Bi_2Se_3@N-C coated separator exhibits a significantly lower voltage polarization (ΔV = 380 mV) compared to the cell paired with the pristine separator (ΔV = 530 mV). Furthermore, the first three CV cycles for both separator configurations indicate coinciding curves, reflecting promising redox processes with high reversibility. However, the extent of reversibility and kinetics is superior for the cell employing 3D Bi_2Se_3@N-C [Figure 3B] interlayer compared to the pristine separator [Supplementary Figure 9].

To validate the CV results, the initial Galvanostatic charge-discharge (GCD) characteristics were examined at 0.05 C, as shown in Figure 3C. The voltage profiles for both the separator configurations exhibit similar shapes, with two distinct reduction voltage regions and a sloppy charging plateau, reflecting the multistep electrochemical processes. This observation aligns well with CV results. However, differences in the extent of the redox plateaus suggest varying extents of redox reactions within the cells. Notably, the cell incorporating the 3D Bi_2Se_3@N-C-modified separator demonstrates the lengthiest redox plateau and the lowermost polarization (ΔE). The ΔE values, presented in Supplementary Figure 8B, reveal that the 3D Bi_2Se_3@N-C coated separator exhibits significantly lower polarization (ΔE = 215 mV) compared to the cell featuring the pristine separator (ΔE = 231 mV). To gain deeper insights, two variables, Q1 and Q2, along with their relative ratio (Q2/Q1), were also evaluated. Here, Q1 measures discharge capacity (with 419 mA h g^{-1} as the theoretical value) corresponding to the first reduction plateau followed by the sloppy region. Likewise, Q2 corresponds to the discharge capacity (with 1,256 mA h g^{-1} as the theoretical value) linked to the second reduction plateau and its sloping region, reflecting the efficiency of the conversion reaction of LiPS to Li_2S[21]. A high relative ratio (Q2/Q1; theoretical value: 3) indicates the conversion efficiency of the designed sample[20]. As presented in Supplementary Figure 8B, the cell featuring the 3D Bi_2Se_3@N-C coated separator reveals a higher ratio (2.65) in contrast to the pristine separator (2.05). This finding highlights the enhanced electrocatalytic activity of the 3D Bi_2Se_3@N-C coated separator toward LiPS species. Consequently, a high initial discharge capacity of 1,132 mA h g^{-1} was delivered by the cell incorporating the 3D Bi_2Se_3@N-C coated separator, equivalent to 67.6% of the theoretical value. In contrast, the cell with the pristine separator achieves only 681 mA h g^{-1} or 40.7% of the theoretical limit. The significantly higher discharge capacity value of the cell utilizing 3D Bi_2Se_3@N-C coated separator underscores its ability to facilitate kinetically favored redox reactions. This performance is attributed to the efficient trapping and catalytic conversion of polysulfide species, leading to enhanced active material utilization.

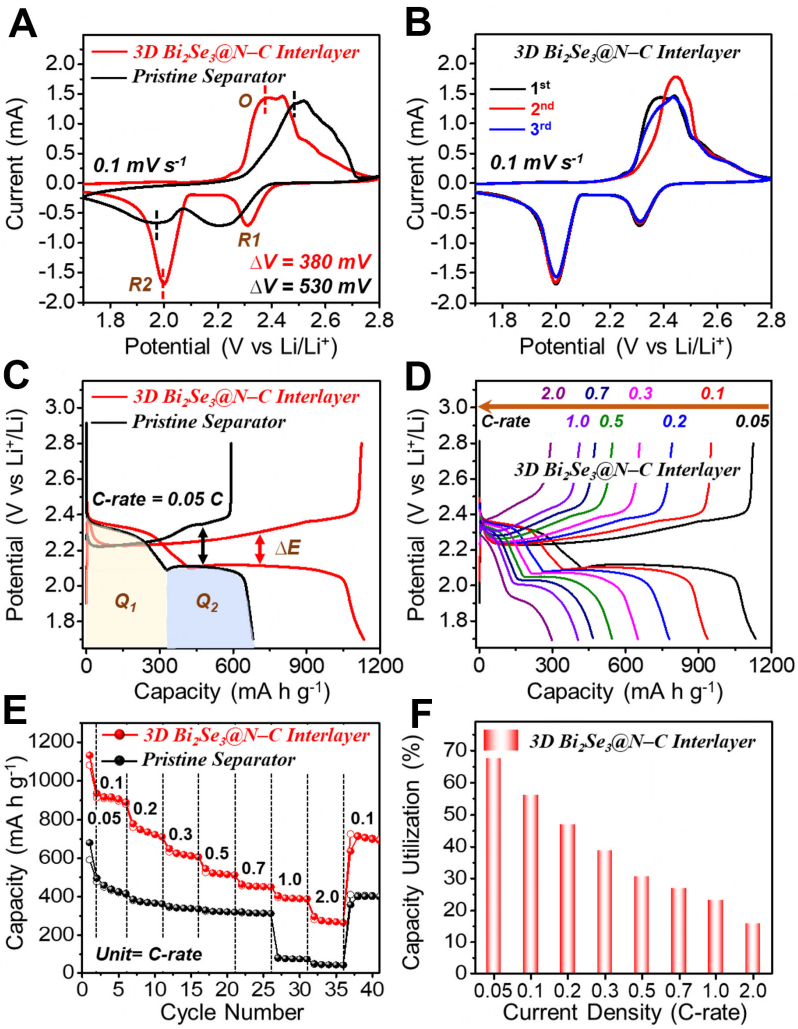

Figure 3. (A) CV profiles of cells paired with coated/pristine separator at 0.1 mV s^{-1}; (B) first three CV scans for cell paired with 3D Bi_2Se_3@N-C coated separator; (C) initial Galvanostatic charge-discharge voltage profile comparison at 0.05 C; (D) charge-discharge voltage profiles at different C-rates with 3D Bi_2Se_3@N-C coated separator; (E) rate performance at various C-rates; and (F) capacity utilization values for 3D Bi_2Se_3@N-C coated separator. CV: Cyclic voltammetry; 3D: three-dimensional.

Rate capability tests were conducted at various current values ranging from 0.05-2.0 C, as shown in Figure 3D and E. The GCD curves at different C-rates for cell paired with 3D Bi_2Se_3@N-C coated separator exhibit well-defined charge-discharge redox plateaus even at 2.0 C-rate, highlighting superior performance compared to the cell with the pristine separator [Supplementary Figure 10]. For the 3D Bi_2Se_3@N-C modified separator, initial capacities of 1134 (0.05 C), 936 (0.1 C), 780 (0.2 C), 650 (0.3 C), 545 (0.5 C), 465 (0.7 C), 405 (1.0 C), and 297 (2.0 C) mA h g^{-1} were achieved. Contrariwise, the cell with the uncoated separator delivered significantly lower discharge capacities of 681 mA h g^{-1}, 495 mA h g^{-1}, 386 mA h g^{-1}, 349 mA h g^{-1}, 330 mA h g^{-1}, 321 mA h g^{-1}, 81 mA h g^{-1}, and 49 mA h g^{-1}, at the same C-rates, as illustrated in Figure 3E. Furthermore, when the current was reversed to 0.1 C, the cell with the 3D Bi_2Se_3@N-C coated separator retained a stable discharge capacity of 694 mA h g^{-1}, significantly higher than the 401 mA h g^{-1} observed for the pristine separator, indicating the excellent reversibility of the redox processes. The proportion of material utilized in redox reactions was measured through capacity utilization (%) parameter, as presented in Figure 3F and Supplementary Figure 11. As expected, the cell paired with a 3D Bi_2Se_3@N-C coated separator demonstrated the maximum capacity utilization values at all C-rates compared to the cell

with the pristine separator. This observation is well synchronized with the CV results, which indicated lower polarization and superior electrocatalytic conversion efficiency.

Stable cycling performance is a critical factor for the commercial viability of the prepared nanostructure. Figure 4A-C illustrates the cycling performance tests of the 3D Bi_2Se_3@N-C coated separator compared to the pristine separator. At a 0.1 C-rate [Figure 4A], 3D Bi_2Se_3@N-C-modified separator exhibits an early discharge capacity of 1,039 mA h g^{-1} and retains 83% (863 mA h g^{-1}) after 100 continuous charge-discharge cycles, corresponding to an average capacity decay rate of just 0.16% per cycle. Moreover, the high Columbic efficiency (~99%) indicates highly reversible redox processes. Conversely, the pristine separator shows a significantly lower initial capacity of 510 mA h g^{-1} (30% of theoretical) and retains only 379 mA h g^{-1} (74% retention) after 100 cycles, corresponding to a higher capacity decay rate of 0.27% per cycle. Similar trends are observed at higher C-rates. For example, at 0.5 C [Figure 4B], a 3D Bi_2Se_3@N-C-coated separator achieves a discharge capacity of 440 mA h g^{-1} after 200 cycles, compared to just 229 mA h g^{-1} for the pristine separator cell. At an even higher C-rate of 2.0 C [Figure 4C], the discharge capacities at the end of the 500th cycle are 219 mA h g^{-1} for the 3D Bi_2Se_3@N-C coated separator and only 62 mA h g^{-1} for the pristine separator. The excellent capacity retention, even after prolonged cycling, underscores the structural merits of the prepared sample. To further access practical viability, cells were assembled with high S-loading electrodes (2.5 and 3.5 mg cm^{-2}). The cycling performance results at 0.3 C-rate are presented in Figure 4D. Even at high sulfur loadings, the cells demonstrate stable cycling up to 200 cycles. For instance, with a sulfur loading of 2.5 mg cm^{-2}, the cell achieves an initial discharge capacity of 579 mA h g^{-1} and retains 58% (337 mA h g^{-1}) of its capacity after 200 cycles. Likewise, at a sulfur loading of 3.5 mg cm^{-2}, the cell retains 57% of its initial capacity, further validating the applicability of the prepared nanostructure for practical applications. These results clearly validate that the manifestation of Bi_2Se_3 nanocrystals significantly enhances the catalytic transformation of anchored polysulfide species, improving active material consumption. Additionally, the N-doping within the nanostructures expedites rapid charge kinetics, resulting in faster redox activity and hence, improved electrochemical performance. The detailed working mechanism of the 3D Bi_2Se_3@N-C coated separator as a polysulfide barrier is schematically demonstrated in Figure 4E. Furthermore, the electrochemical performance results obtained in this study are summarized in Supplementary Table 2 and benchmarked against previously published works. Furthermore, high gravimetric energy density for Li-S cells utilizing different sulfur loadings and 3D Bi_2Se_3@N-C interlayers [Supplementary Table 3] again indicates the practical application potential of this strategy.

The enhanced redox kinetics of the 3D Bi_2Se_3@N-C coated separator were analyzed by determining the diffusion coefficient (D_{Li^+}) values. CV measurements were performed on cells with 3D Bi_2Se_3@N-C coated and pristine separator at different scan rates (0.05 mV s^{-1} to 1.0 mV s^{-1}), as revealed in Figure 5A and B. The D_{Li^+} values were calculated by plotting the I_p (peak current) against the $v^{0.5}$ (scan rate square root), based on the Randles-Sevick equation[48]:

$$I_p = 2.69 \times 10^5 n^{1.5} A D_{Li^+}{}^{0.5} C_{Li} v^{0.5} \quad (1)$$

where I_p represents the redox peak current, n is the number of electrons involved, A is the electrode surface area (cm^2), C_{Li} is the concentration (mol L^{-1}) of Li-ion, and v is the voltage scan rate (Vs^{-1}). The CV curves for cell featuring the 3D Bi_2Se_3@N-C coated separator [Figure 5A] exhibit two distinct reduction peaks (R1/R2) and one oxidation peak (O), even at high voltage scan rates, indicating enhanced redox reaction kinetics. In contrast, the cell with the pristine separator [Figure 5B] displays poorly resolved reduction peaks at high scan rates, reflecting sluggish reaction kinetics. Additionally, the more symmetric CV curves and high current intensity observed for the 3D Bi_2Se_3@N-C coated separator highlight faster Li-ion diffusion.

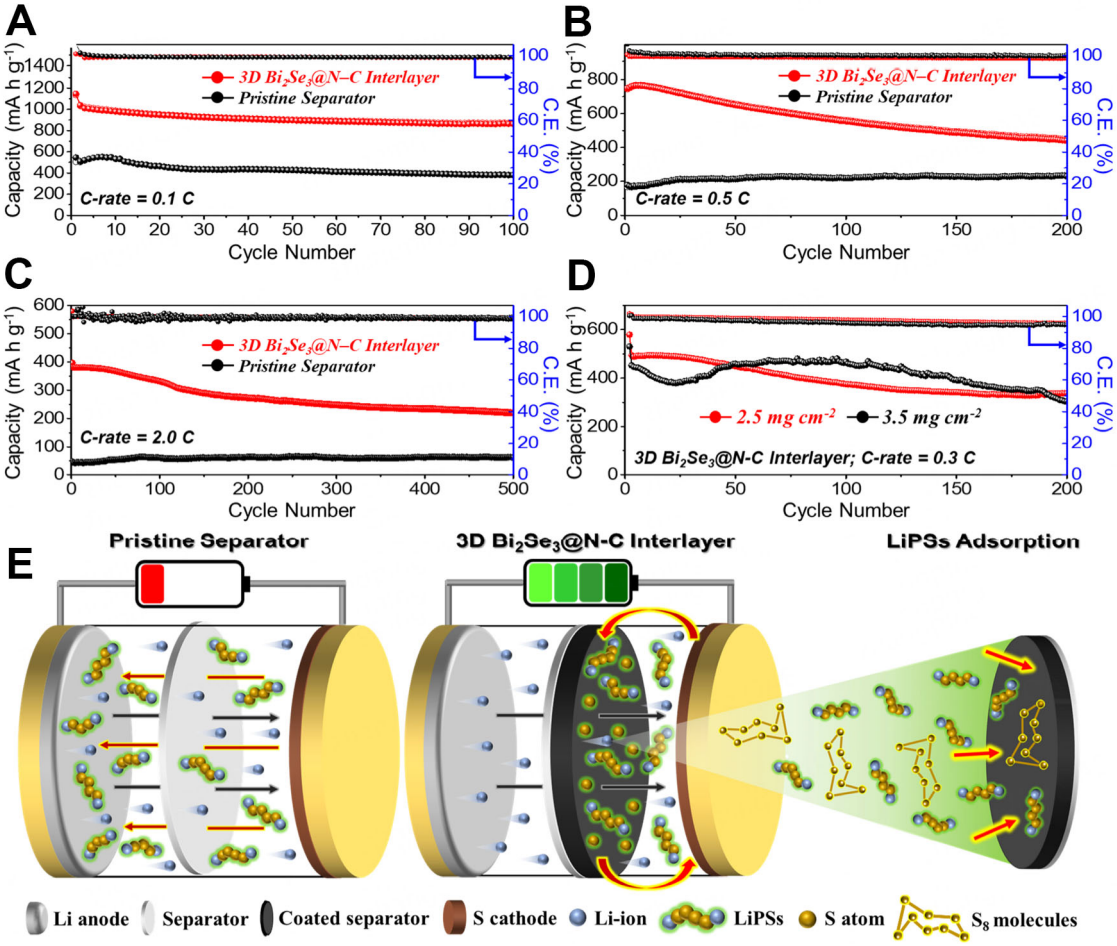

Figure 4. Cycling tests of cells featuring coated/pristine separators at (A) 0.1 C-rate; (B) 0.5 C-rate; (C) 2.0 C-rate; (D) cycling test of 3D Bi_2Se_3@N-C at 0.3 C coupled with high loading electrodes; and (E) detailed working mechanism of the 3D Bi_2Se_3@N-C modified separator. 3D: Three-dimensional.

The D_{Li^+} values for the Li-S cell with a 3D Bi_2Se_3@N-C coated separator were approximately 1.5 × 10^{-7} cm^2 s^{-1}, 0.3 × 10^{-7} cm^2 s^{-1}, and 0.6 × 10^{-7} cm^2 s^{-1} for peaks O, R1, and R2, respectively [Figure 5C]. In comparison, the pristine separator cell showed significantly lower D_{Li^+} values of 2.3 × 10^{-8} cm^2 s^{-1}, 0.4 × 10^{-8} cm^2 s^{-1}, and 1.6 × 10^{-8} cm^2 s^{-1} for peaks O, R1, and R2, respectively [Figure 5D]. These higher D_{Li^+} values underscore the structural merits of the 3D Bi_2Se_3@N-C microspheres, which effectively trap and catalytically convert polysulfide while the highly conductive N-C framework facilitates electron transfer by lowering the charge-transfer resistance (R_{ct}), thereby boosting the electrochemical properties. To further evaluate the interfacial surface processes taking place at electrode-separator-electrolyte boundaries, Nyquist plots were plotted via electrochemical impedance spectroscopy (EIS) both before [Figure 5E] and after cycling [Figure 5F]. The data was fitted using an equivalent circuit model [Supplementary Figure 12]. Before cycling, the impedance measurements at open-circuit voltage revealed negligible solution resistance (R_s) values of 3-5 Ω for both cells, indicating a similar electrolyte-electrode interface. However, the R_{ct} for the cell with a 3D Bi_2Se_3@N-C coated separator was significantly lower (~45 Ω) compared to the uncoated separator (~80 Ω), suggesting enhanced Li-ion kinetics. After 500 cycles at a 2.0 C-rate, the R_{ct} for the 3D Bi_2Se_3@N-C coated separator cell decreases significantly to ~17 Ω, demonstrating enhanced kinetics over prolonged cycling. Conversely, the uncoated separator cell demonstrates a marginal reduction in R_{ct} to ~66 Ω, indicating poor diffusion kinetics primarily due to uncontrolled polysulfide migration and the formation of

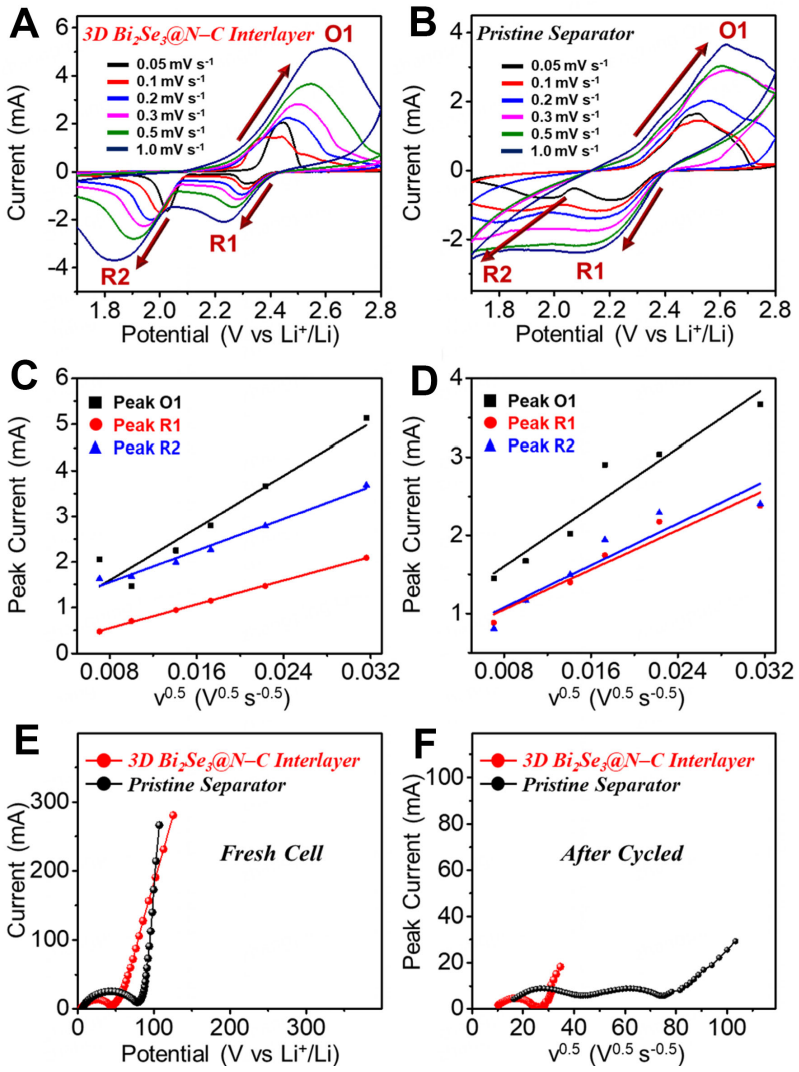

Figure 5. D_{Li^+} coefficient and EIS plots for coated/pristine separators: (A and B) CV curves at different scan rates (0.05-1.0 mV s^{-1}); (C and D) redox peak intensity vs. square root of scan rate; (E) EIS plots of newly assembled cell; and (F) after 300 cycles at 2.0 C. CV: Cyclic voltammetry; EIS: electrochemical impedance spectroscopy.

inactive materials that hinder reaction efficiency. This behavior is further supported by the presence of two distinct semicircles in the EIS curve of the pristine separator cell after cycling, with the high-frequency semicircle attributed to the insulating layer of solid Li_2S_2/Li_2S[49]. In contrast, the 3D Bi_2Se_3@N-C coated separator suppressed polysulfide diffusion, as evidenced by a single semicircle in the EIS plot. These findings validate the structural superiority of the 3D Bi_2Se_3@N-C microspheres, which provide outstanding charge transfer features, diminish cell resistance, effectively trap and catalyze polysulfide molecules, and enhance sulfur consumption during prolonged cycling. The efficient trapping of the polysulfide was also confirmed through perceivable polysulfide adsorption tests [Supplementary Figure 13]. A continuous fading of solution color containing 3D Bi_2Se_3@N-C microspheres from yellow to translucent (T = 1 h), signifying effective anchoring of the LiPSs. To further validate this, the cell comprising 3D Bi_2Se_3@N-C microspheres as the coated interlayer was disassembled carefully inside the glove box after cycling at 2.0 C and the interlayer was analyzed using FE-SEM. The micrographs shown in Supplementary Figure 14A and B demonstrate that the spherical morphology of the cycled separator remained intact even after prolonged

cycling (500 cycles). Furthermore, no evidence of polysulfide agglomeration was found on the spherical surface, indicating the effective electrocatalytic conversion of the trapped LiPS species.

Overall, the enhancement in electrochemical properties of cells retaining 3D Bi_2Se_3@N-C microspheres as a multifunctional polysulfide barrier firmly validates the structural supremacy of the prepared nanostructures that resulted in improved redox reaction kinetics via fast charge transfer characteristics, suppress polysulfide diffusion, and enhance active sulfur participation during electrochemical processes.

CONCLUSIONS

In conclusion, this work presents a comprehensive study on the synthesis of 3D Bi_2Se_3@N-C microspheres and their application as a multifunctional polysulfide barrier for improved LSB properties such as realistic rate capability and steady cycling performance across a range of C-rates, from low (0.1 C and 0.5 C) to high (2.0 C). The incorporation of Bi_2Se_3 nanocrystals ensures efficient anchoring and transformation of polysulfide, enhancing sulfur participation in electrochemical reactions. Furthermore, N-doping within the carbon framework expedites rapid charge transferal, accelerating redox activity. As a result, the cell equipped with a 3D Bi_2Se_3@N-C microsphere coated separator delivered remarkable performance, including high rate properties (297 mA h g^{-1} at 2.0 C-rate) and prolonged stable cycling performance at different C-rates (863 mA h g^{-1} after 100 cycles at 0.1 C, 440 mA h g^{-1} after 200 cycles at 0.5 C, and 219 mA h g^{-1} after 500 cycles at 2.0 C). Additionally, even at a loading of 3.5 mg cm^{-2}, the cell maintained satisfactory cycling performance, retaining 57% of its capacity after 200 charge-discharge cycles.

DECLARATIONS

Authors' contributions

Substantial contributions to the conception and design of the study, data analysis and interpretation: Saroha, R.
Substantial contributions to the conception and design of the study, data interpretation, and blueprint preparation: Lee, J. S.
Data acquisition: Cho, S. W.
Administrative and material support, writing-review and editing: Cho, C.
Technical and material support, writing and review: Park, J. S.
Supervision of the work, administrative, technical, and material support, writing-review and editing: Cho, J. S.

Availability of data and materials

The rata data supporting the findings of this study are available within this Article and its Supplementary Materials file.

Financial support and sponsorship

This work was supported by the National Research Foundation of Korea (NRF) grant funded by the Korea government (MSIT) (Grant No. RS-2023-00217581, RS-2025-00556955). It was also supported by the Technology Development Program (RS-2023-00263878) funded by the Ministry of SMEs and Startups (MSS, Korea). Additionally, this research was supported by the Global - Learning & Academic Research Institution for Master's, PhD students, and Postdocs (G-LAMP) Program of the NRF grant funded by the Ministry of Education (No. RS-2023-00285390).

Conflicts of interest

All authors declared that there are no conflicts of interest.

Ethical approval and consent to participate

Not applicable.

Consent for publication

Not applicable.

REFERENCES

1. Manthiram, A.; Fu, Y.; Su, Y. S. Challenges and prospects of lithium-sulfur batteries. *Acc. Chem. Res.* **2013**, *46*, 1125-34. DOI PubMed
2. Zhou, L.; Li, H.; Wu, X.; et al. Double-shelled Co_3O_4/C nanocages enabling polysulfides adsorption for high-performance lithium-sulfur batteries. *ACS. Appl. Energy. Mater.* **2019**, *2*, 8153-62. DOI
3. Zhao, M.; Li, B. Q.; Zhang, X. Q.; Huang, J. Q.; Zhang, Q. A perspective toward practical lithium-sulfur batteries. *ACS. Cent. Sci.* **2020**, *6*, 1095-104. DOI
4. Wang, Z.; Wang, B.; Yang, Y.; et al. Mixed-metal-organic framework with effective lewis acidic sites for sulfur confinement in high-performance lithium-sulfur batteries. *ACS. Appl. Mater. Interfaces.* **2015**, *7*, 20999-1004. DOI
5. Wang, P.; Zeng, R.; You, L.; et al. Graphene-like matrix composites with Fe_2O_3 and Co_3O_4 as cathode materials for lithium-sulfur batteries. *ACS. Appl. Nano. Mater.* **2020**, *3*, 1382-90. DOI
6. Pope, M. A.; Aksay, I. A. Structural design of cathodes for Li-S batteries. *Adv. Energy. Mater.* **2015**, *5*, 1500124. DOI
7. Kim, J.; Lee, D.; Jung, H.; Sun, Y.; Hassoun, J.; Scrosati, B. An advanced lithium-sulfur battery. *Adv. Funct. Mater.* **2013**, *23*, 1076-80. DOI
8. He, G.; Evers, S.; Liang, X.; Cuisinier, M.; Garsuch, A.; Nazar, L. F. Tailoring porosity in carbon nanospheres for lithium-sulfur battery cathodes. *ACS. Nano.* **2013**, *7*, 10920-30. DOI PubMed
9. Li, Z.; Jiang, Y.; Yuan, L.; et al. A highly ordered meso@microporous carbon-supported sulfur@smaller sulfur core-shell structured cathode for Li-S batteries. *ACS. Nano.* **2014**, *8*, 9295-303. DOI
10. Sun, L.; Wang, D.; Luo, Y.; et al. Sulfur embedded in a mesoporous carbon nanotube network as a binder-free electrode for high-performance lithium-sulfur batteries. *ACS. Nano.* **2016**, *10*, 1300-8. DOI
11. Chulliyote, R.; Hareendrakrishnakumar, H.; Joseph, M. G. Hierarchical porous carbon material with multifunctionalities derived from honeycomb as a sulfur host and laminate on the cathode for high-performance lithium-sulfur batteries. *ACS. Sustainable. Chem. Eng.* **2019**, *7*, 19344-55. DOI
12. Zhang, F.; Li, Z.; Cao, T.; et al. Multishelled Ni_2P microspheres as multifunctional sulfur host 3D-printed cathode materials ensuring high areal capacity of lithium-sulfur batteries. *ACS. Sustainable. Chem. Eng.* **2021**, *9*, 6097-106. DOI
13. Park, J.; Yu, B. C.; Park, J. S.; et al. Tungsten disulfide catalysts supported on a carbon cloth interlayer for high performance Li-S battery. *Adv. Energy. Mater.* **2017**, *7*, 1602567. DOI
14. Liu, Z.; Sun, L.; Liu, X.; Lu, Q. Stabilization strategies of lithium metal anode toward dendrite-free lithium-sulfur batteries. *Chem. Eur. J.* **2024**, *30*, e202402032. DOI
15. Song, B.; Su, L.; Liu, X.; et al. An examination and prospect of stabilizing Li metal anode in lithium-sulfur batteries: a review of latest progress. *Electron* **2023**, *1*, e13. DOI
16. Song, J.; Xu, T.; Gordin, M. L.; et al. Nitrogen-doped mesoporous carbon promoted chemical adsorption of sulfur and fabrication of high-areal-capacity sulfur cathode with exceptional cycling stability for lithium-sulfur batteries. *Adv. Funct. Mater.* **2014**, *24*, 1243-50. DOI
17. Chung, S.; Manthiram, A. Bifunctional separator with a light-weight carbon-coating for dynamically and statically stable lithium-sulfur batteries. *Adv. Funct. Mater.* **2014**, *24*, 5299-306. DOI
18. Xu, R.; Lu, J.; Amine, K. progress in mechanistic understanding and characterization techniques of Li-S batteries. *Adv. Energy. Mater.* **2015**, *5*, 1500408. DOI
19. Liu, Y.; Elias, Y.; Meng, J.; et al. Electrolyte solutions design for lithium-sulfur batteries. *Joule* **2021**, *5*, 2323-64. DOI
20. Saroha, R.; Choi, H. H.; Cho, J. S. Boosting redox kinetics using rationally engineered cathodic interlayers comprising porous rGO-CNT framework microspheres with $NiSe_2$-core@N-doped graphitic carbon shell nanocrystals for stable Li-S batteries. *Chem. Eng. J.* **2023**, *473*, 145391. DOI
21. Saroha, R.; Ka, H. S.; Park, G. D.; Cho, C.; Kang, D.; Cho, J. S. Long-term stability of lithium-sulfur batteries via synergistic integration of nitrogen-doped graphitic carbon-coated cobalt selenide nanocrystals within porous three-dimensional graphene-carbon nanotube microspheres. *J. Power. Sources.* **2024**, *592*, 233893. DOI
22. Wang, L.; Meng, X.; Wang, X.; Zhen, M. Dual-conductive $CoSe_2$@$TiSe_2$ -C heterostructures promoting overall sulfur redox kinetics under high sulfur loading and lean electrolyte. *Small* **2023**, *19*, 2300089. DOI
23. Lu, J.; Luo, S.; Qi, Z.; et al. Recent advances in transition metal chalcogenide derivatives from metal-organic frameworks for lithium-

sulfur batteries. *Cell. Rep. Phys. Sci.* **2024**, *5*, 102028. DOI

24. Shirodkar, S. N.; Dev, P. Nonlinear hybrid surface-defect states in defective Bi_2Se_3. *J. Phys. Chem. C.* **2022**, *126*, 11833-9. DOI
25. Zhang, H.; Liu, C.; Qi, X.; Dai, X.; Fang, Z.; Zhang, S. Topological insulators in Bi_2Se_3, Bi_2Te_3 and Sb_2Te_3 with a single Dirac cone on the surface. *Nature. Phys.* **2009**, *5*, 438-42. DOI
26. Xia, Y.; Qian, D.; Hsieh, D.; et al. Observation of a large-gap topological-insulator class with a single Dirac cone on the surface. *Nature. Phys.* **2009**, *5*, 398-402. DOI
27. Hu, L.; Zhu, T.; Liu, X.; Zhao, X. Point defect engineering of high-performance bismuth-telluride-based thermoelectric materials. *Adv. Funct. Mater.* **2014**, *24*, 5211-8. DOI
28. Singh, S.; Sahoo, R. K.; Shinde, N. M.; et al. Asymmetric faradaic assembly of Bi_2O_3 and MnO_2 for a high-performance hybrid electrochemical energy storage device. *RSC. Adv.* **2019**, *9*, 32154-64. DOI
29. Wang, K.; Shao, C.; Li, X.; Miao, F.; Lu, N.; Liu, Y. Heterojunctions of p-BiOI nanosheets/n-TiO_2 nanofibers: preparation and enhanced visible-light photocatalytic activity. *Materials* **2016**, *9*, 90. DOI PubMed PMC
30. El-makaty, F. M.; Nawaz, M.; Shakoor, R.; Hammuda, A.; Youssef, K. M. Microstructural effect on the corrosion behavior of n- and p-type bismuth tellurides fabricated by induction melting. *Mater. Charact.* **2023**, *202*, 112987. DOI
31. Cho, W. S.; Hong, D. M.; Dong, W. J.; et al. Porously reduced 2-dimensional $Bi_2O_2CO_3$ petals for strain-mediated electrochemical CO_2 reduction to HCOOH. *Energy. Environ. Mater.* **2024**, *7*, e12490. DOI
32. Abzal, S. M.; Khatua, S.; Kalyan, K.; et al. Exploring the electrochemical performance of layered Bi_2Se_3 hexagonal platelets as the anode material for lithium-ion batteries. *Phys. Chem. Chem. Phys.* **2024**, *26*, 25418-29. DOI
33. Gao, L.; Li, H.; Ren, W.; et al. Patterning Bi_2Se_3 single-crystalline thin films on Si(111) substrates using strong oxidizing acids. *RSC. Adv.* **2017**, *7*, 32294-9. DOI
34. Edmonds, M. T.; Hellerstedt, J. T.; Tadich, A.; et al. Stability and surface reconstruction of topological insulator Bi_2Se_3 on exposure to atmosphere. *J. Phys. Chem. C.* **2014**, *118*, 20413-9. DOI
35. Kong, D.; Cha, J. J.; Lai, K.; et al. Rapid surface oxidation as a source of surface degradation factor for Bi_2Se_3. *ACS. Nano.* **2011**, *5*, 4698-703. DOI
36. Dharmadhikari, V. S.; Sainkar, S.; Badrinarayan, S.; Goswami, A. Characterisation of thin films of bismuth oxide by X-ray photoelectron spectroscopy. *J. Electron. Spectrosc. Relat. Phenom.* **1982**, *25*, 181-9. DOI
37. Wu, J.; Zhao, J.; Vaidhyanathan, B.; et al. Rapid microwave-assisted bulk production of high-quality reduced graphene oxide for lithium ion batteries. *Materialia* **2020**, *13*, 100833. DOI
38. Varodi, C.; Pogăcean, F.; Ciorița, A.; et al. Nitrogen and sulfur co-doped graphene as efficient electrode material for L-cysteine detection. *Chemosensors* **2021**, *9*, 146. DOI
39. Begum, H.; Ahmed, M. S.; Jeon, S. New approach for porous chitosan-graphene matrix preparation through enhanced amidation for synergic detection of dopamine and uric acid. *ACS. Omega.* **2017**, *2*, 3043-54. DOI PubMed PMC
40. Ismagilov, Z. R.; Shalagina, A. E.; Podyacheva, O. Y.; et al. Structure and electrical conductivity of nitrogen-doped carbon nanofibers. *Carbon* **2009**, *47*, 1922-9. DOI
41. Sun, H.; Xiao, M.; Zhu, F. Nitrogen doped porous carbon with high rate performance for lithium ion storage. *J. Electroanal. Chem.* **2023**, *932*, 117254. DOI
42. Nulu, A.; Nulu, V.; Sohn, K. Y. N-doped CNTs wrapped sulfur-loaded hierarchical porous carbon cathode for Li-sulfur battery studies. *RSC. Adv.* **2024**, *14*, 2564-76. DOI PubMed PMC
43. Lee, J. Y.; Kim, N. Y.; Shin, D. Y.; et al. Nitrogen-doped graphene-wrapped iron nanofragments for high-performance oxygen reduction electrocatalysts. *J. Nanopart. Res.* **2017**, *19*, 98. DOI
44. Li, Y.; Jiang, T.; Yang, H.; et al. A heterostuctured Co_3S_4/MnS nanotube array as a catalytic sulfur host for lithium-sulfur batteries. *Electrochim. Acta.* **2020**, *330*, 135311. DOI
45. Tang, H.; Yao, S.; Xue, S.; et al. In-situ synthesis of carbon@Ti_4O_7 non-woven fabric as a multi-functional interlayer for excellent lithium-sulfur battery. *Electrochim. Acta.* **2018**, *263*, 158-67. DOI
46. Yu, R.; Chung, S.; Chen, C.; Manthiram, A. An ant-nest-like cathode substrate for lithium-sulfur batteries with practical cell fabrication parameters. *Energy. Storage. Mater.* **2019**, *18*, 491-9. DOI
47. Xiang, Y.; Li, J.; Lei, J.; et al. Advanced Separators for lithium-ion and lithium-sulfur batteries: a review of recent progress. *ChemSusChem* **2016**, *9*, 3023-39. DOI
48. Kim, G.; Lee, Y.; Park, J.; et al. Enhanced performance of lithium-sulfur battery cathode via composition optimization using modified MWCNTs as a conductive material and poly (acrylic acid) as a binder. *Int. J. Electrochem. Sci.* **2023**, *18*, 100217. DOI
49. Ghazi, Z. A.; He, X.; Khattak, A. M.; et al. MoS2/celgard separator as efficient polysulfide barrier for long-life lithium-sulfur batteries. *Adv. Mater.* **2017**, *29*, 1606817. DOI